

# Dynamic topology in spatiotemporal chaos

Nicholas T. Ouellette<sup>1</sup> and J. P. Gollub<sup>1,2,a)</sup>

<sup>1</sup>Department of Physics, Haverford College, Haverford, Pennsylvania 19041, USA

<sup>2</sup>Department of Physics, University of Pennsylvania, Philadelphia, Pennsylvania 19104, USA

(Received 25 February 2008; accepted 19 May 2008; published online 30 June 2008)

By measuring the tracks of tracer particles in a quasi-two-dimensional spatiotemporally chaotic laboratory flow, we determine the instantaneous curvature along each trajectory and use it to construct the instantaneous curvature field. We show that this field can be used to extract the time-dependent hyperbolic and elliptic points of the flow. These important topological features are created and annihilated in pairs only above a critical Reynolds number that is largest for highly symmetric flows. We also study the statistics of curvature for different driving patterns and show that the curvature probability distribution is insensitive to the details of the flow. © 2008 American Institute of Physics. [DOI: [10.1063/1.2948849](https://doi.org/10.1063/1.2948849)]

## I. INTRODUCTION

Fluid systems provide excellent opportunities for studying spatiotemporal chaos (STC).<sup>1,2</sup> A system displaying STC is, in general, governed by partial differential equations and has in principle an infinite number of degrees of freedom in the continuum approximation. If a sufficiently large number of degrees of freedom are excited, the system is turbulent. But if only a subset of these degrees of freedom is active, so that the flow lacks a turbulent cascade, the dynamics instead may be said to be spatiotemporally chaotic. Often, the number of active degrees of freedom is proportional to the system size; that is, STC is extensive.<sup>3–5</sup>

Classic examples of STC in fluids include spiral defect chaos in thermal convection<sup>2,5–7</sup> and irregularly moving localized structures in electrically driven liquid crystal layers.<sup>8</sup> It is usually understood that in STC, spatial structures must be deformed in ways that are nonperiodic in time; exactly how this occurs, however, remains unclear.

In this paper, we address the question of how the spatial structures are modified and evolve as a flow becomes spatiotemporally chaotic. We do so by looking at topological properties of the velocity field.

The fundamental quantity of interest in any fluid flow is the velocity field. As is the case for any vector field, locations where the magnitude of the field vanishes have special topological significance. At these stagnation points (also called critical points, in the context of nonlinear dynamics<sup>9</sup>), the direction of the velocity field is undefined. To a large extent, the qualitative structure of the flow is determined by the locations of the stagnation points and the local flow around each of them.

In a two-dimensional incompressible flow field, there are only two possible types of stagnation points. In regions of strong vorticity, where the flow is highly rotational, a stagnation point is elliptic. As sketched in Fig. 1, the instantaneous local flow around an elliptic point consists of concentric closed streamlines. Stagnation points in straining

regions, however, are hyperbolic. Figure 1 also shows the instantaneous local flow around a hyperbolic point, which is dominated by four special streamlines that meet at the hyperbolic point; two of these streamlines bring fluid to the hyperbolic point (the stable manifold), while the other two carry fluid away (the unstable manifold). In a time-dependent flow, both the streamlines and the locations of the hyperbolic and elliptic points change in time; nevertheless, the qualitative flows around the hyperbolic and elliptic points persist.

We recently described a method for locating these hyperbolic and elliptic points in two-dimensional flows by considering the curvature of the trajectories of tracer particles.<sup>10</sup> We showed that for sufficiently strong driving, the hyperbolic and elliptic points break free from their forced locations and began to interact, undergoing annihilation and creation in hyperbolic-elliptic pairs. These interactions begin abruptly at a finite driving strength.

Here, we describe the curvature fields and the dynamics of the hyperbolic and elliptic points for three quasi-two-dimensional base flows with different imposed symmetries: the square vortex lattice we considered previously,<sup>10</sup> forcing that is random in space,<sup>11,12</sup> and a set of parallel shear bands (commonly known as the Kolmogorov flow<sup>13</sup>). We investigate how the degree of spatial symmetry of the flow forcing affects the onset of topological changes as the Reynolds number is varied.

We begin in Sec. II by describing our experimental methods, including an improved procedure for locating the hyperbolic and elliptic points that is able to handle flow fields with strong shear correctly. In Sec. III, we present our results, discussing both statistics of the curvature field and the dynamics of the hyperbolic and elliptic points. We find that the probability density function (PDF) of curvature is extremely wide, and that its shape is independent of Reynolds number when properly rescaled. Surprisingly, this shape can be described by a model that considers the flow velocity and acceleration to be Gaussian random variables. By tracking the motion of the hyperbolic and elliptic points, we show that topological changes of the flow field, indicated by pairwise creation and annihilation of hyperbolic and el-

<sup>a)</sup>Electronic mail: [jgollub@haverford.edu](mailto:jgollub@haverford.edu).

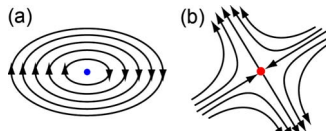


FIG. 1. (Color online) Sketch of the local flows around (a) an elliptic point and (b) a hyperbolic point.

lptic points, occur only above a finite Reynolds number for all three flows considered. This critical driving is greatest for flows with the greatest forcing symmetry. We also show that these creation and annihilation events appear to be uncorrelated with the forcing structure, occurring at random spatial locations. Finally, in Sec. IV, we conclude and offer some suggestions for future research.

## II. METHODOLOGY

### A. Experimental flow and particle tracking

To generate a quasi-two-dimensional fluid flow, we drive current through a thin layer of conducting fluid placed over an array of permanent magnets.<sup>10–12,14,15</sup> The Lorentz forces produced by this arrangement generate body forces in the fluid and give rise to flows that can be quite complex. By adjusting the layout of the magnets, we can change the symmetry of the forcing; a sketch of our apparatus and of the three magnet arrays used is shown in Fig. 2. Previous systems of this type have often used alternating currents; here, however, we use a controlled direct current. The strength of the driving is measured by the Reynolds number  $Re=UL/\nu$ , where  $U$  is the root-mean-square fluid velocity,  $L$  is an appropriate length scale (equal to the mean magnet spacing for the random and square magnet arrays and the forcing wavelength for the Kolmogorov flow), and  $\nu$  is the kinematic viscosity. As we vary  $Re$ , we can drive the flow through the transition from a state locked to the magnetic forcing and into the regime of STC. In Fig. 3, we show sample velocity and vorticity fields for our three flows at both the lowest and highest Reynolds numbers measured.

To measure the flow, we track the simultaneous motion of thousands of  $116\text{ }\mu\text{m}$  diameter fluorescent polystyrene

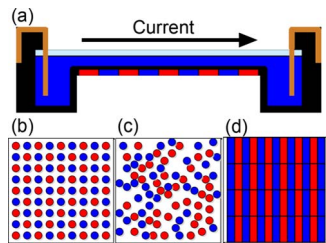


FIG. 2. (Color online) Sketch of (a) the quasi-two-dimensional flow apparatus, as well as the three magnet arrays used in this work: (b) a square lattice, (c) a random array, and (d) a set of parallel linear magnets generating shear bands, also known as the Kolmogorov flow (Ref. 13). As described in the text, the apparatus contains two fluids: a 6-mm-deep layer of heavy fluid underneath a 5-mm-deep layer of light fluid. A square area measuring  $20.3\times 20.3\text{ cm}^2$  is driven, of which the central  $10\times 8.5\text{ cm}^2$  is imaged.

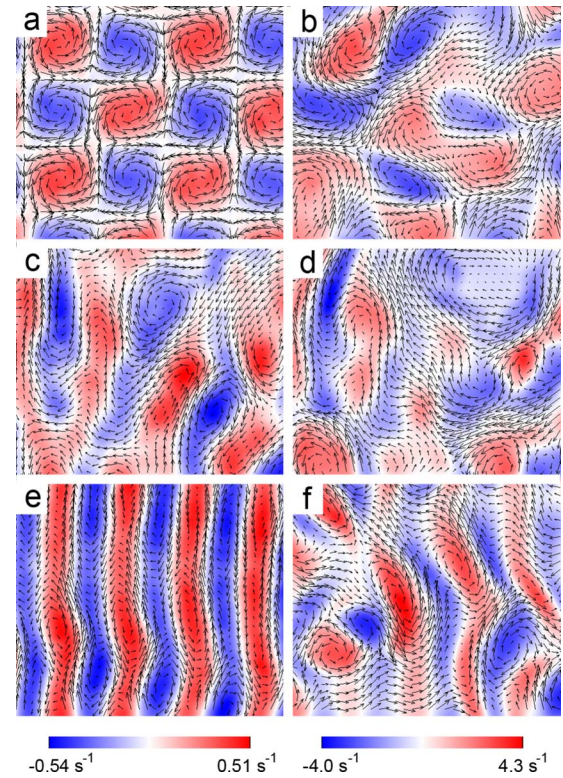


FIG. 3. (Color online) Representative velocity and vorticity fields for each of the three base flows: the square magnet lattice [(a) and (b)], random array [(c) and (d)], and Kolmogorov flow [(e) and (f)]. Data are shown for both “low” (left column) and “high” (right column) Reynolds number: (a)  $Re=28$ , (b)  $Re=182$ , (c)  $Re=21$ , (d)  $Re=168$ , (e)  $Re=30$ , and (f)  $Re=201$ . The velocity field is represented by arrows, while the shading shows the vorticity (counterclockwise rotation is red online). The spatial resolution of the velocity field is actually a factor of 15 greater than shown.

tracer particles.<sup>16</sup> The particles are illuminated by blue light-emitting diodes, and the resulting fluorescence is imaged at a rate of 30 Hz by a complementary metal oxide semiconductor camera. Using a Gaussian estimation scheme,<sup>16</sup> we locate the center of each particle to a precision better than 0.1 pixel, corresponding to roughly  $20\text{ }\mu\text{m}$ . The positions are then fed into a predictive tracking algorithm, and the trajectories of the particles are determined. We extract the velocity and acceleration of each particle using polynomial fits to short track sections.<sup>10,11</sup> The velocity field is then constructed by interpolating between the discrete particle velocities using a Delaunay-triangulation-based linear interpolation scheme. We note that all measurements are taken in the center of the flow so that boundary effects may be neglected.

Our flow is quasi-two-dimensional in that there is essentially no fluid motion in the depth direction, even though the velocity field is different at different depths. In order to ensure that our particles sample only a single plane of the flow, we trap them at the interface between two miscible, stably stratified fluids: a bottom layer (6 mm deep) of a 10% by weight  $\text{CuSO}_4$  solution and a top layer (5 mm deep) of a 2%  $\text{KCl}$  solution. Since the particles are confined to a plane at a single depth, the variation of the velocity in the depth direction does not influence our measurements. Finally, we note that although the two layers are miscible, they remain

distinct on the time scale of our experiments. The layer miscibility is advantageous for us, since the particles therefore experience essentially no surface-tension-driven forces.<sup>17</sup>

## B. Locating hyperbolic and elliptic points

In principle, the hyperbolic and elliptic points of the flow are located at positions where the velocity vanishes (i.e., the stagnation points). Experimentally, however, locating zeros of the velocity field is not possible: since there will always be some level of noise in the measurements, true zeros cannot be measured. If one instead searches for local minima of the velocity field, the results are not robust. To locate the hyperbolic and elliptic points reliably, we therefore turn to an approach based on differential geometry.<sup>10</sup>

Our raw data are particle tracks. In two dimensions, we can describe each trajectory in a local coordinate system defined by a vector  $\mathbf{T}$  tangent to the curve and a vector  $\mathbf{N}$  normal to it. The Frenet formulas give the equations of motion of these vectors along the curve as<sup>18</sup>

$$\frac{d\mathbf{T}}{ds} = \kappa\mathbf{N}, \quad \frac{d\mathbf{N}}{ds} = -\kappa\mathbf{T}, \quad (1)$$

where  $s$  is the arc length and  $\kappa$  is the curvature. In principle, the curvature is a purely geometrical quantity with no dynamical significance. We can, however, write the curvature in terms of easily measurable dynamical quantities as

$$\kappa = \frac{a_n}{u^2}, \quad (2)$$

where  $a_n$  is the acceleration normal to the direction of motion and  $u$  is the magnitude of the velocity.

Consider now the curvature of the trajectory of a fluid element passing near a hyperbolic or elliptic point. In both cases, the fluid element will strongly change its direction of motion over a very short distance, leading to high curvature. We therefore construct the curvature field, whose value at any location in space is the instantaneous curvature of the fluid element passing through that point; the hyperbolic and elliptic points are then located at local maxima of this field.

Other types of local flow, however, may also produce large fluid element curvatures. In particular, as discussed below, regions of high shear often correspond to large curvature, even though they may not contain a hyperbolic or an elliptic point. To isolate the topologically special curvature maxima, then, we apply an additional test, based on the work of Foss.<sup>19</sup> Hyperbolic and elliptic points carry topological charge. This charge can be determined by considering the rotation of the velocity field vector along a closed path surrounding the candidate hyperbolic or elliptic point. If the field vector rotates by  $2\pi$  radians in the same sense as the rotation along the path, the point is elliptic; if instead it rotates by  $2\pi$  radians in the opposite sense, the point is hyperbolic. If the path does not enclose a (net) hyperbolic or elliptic point, the velocity field vector will not undergo a net rotation.<sup>19</sup> By using this test, we can distinguish true hyperbolic and elliptic points from high-shear regions. We note that, as this is a topological test, elliptic points corresponding to both clockwise and counterclockwise vorticity will both

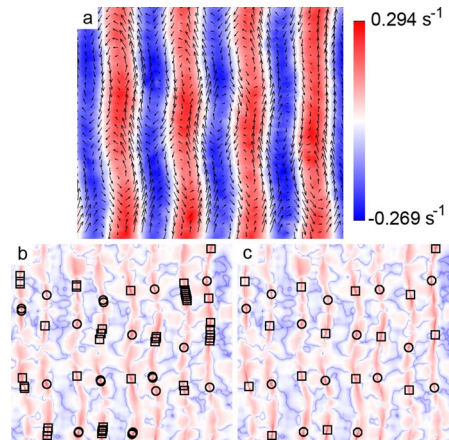


FIG. 4. (Color online) Comparison of our previous (Ref. 10) and new methods for locating hyperbolic and elliptic points. (a) The instantaneous local shear strain rate (shown by the shading) and the velocity field (arrows) for the Kolmogorov flow at  $Re=30$ . (b) The logarithm of the curvature field (shading; red is large online), with the hyperbolic and elliptic points located by our previous method, using a threshold curvature and the Okubo–Weiss parameter (see text for more details). Hyperbolic points are designated by squares and elliptic points by circles. (c) The hyperbolic and elliptic points located by the method of the present paper, which uses both curvature and topological charge. The new method avoids detecting spurious points in regions of high shear, where curvature may be large without the presence of a true hyperbolic or elliptic point.

show a  $+2\pi$  radian vector rotation. To summarize, a local curvature maximum with a negative topological charge is identified as a hyperbolic point, while a local curvature maximum with a positive topological charge is identified as an elliptic point. Local curvature maxima with no net topological charge are rejected.

Previously,<sup>10</sup> we located hyperbolic and elliptic points by first looking for local maxima of the curvature field above some threshold, which we took to be the mean curvature. To distinguish between hyperbolic and elliptic curvature maxima, we used the Okubo–Weiss parameter,<sup>20,21</sup> defined to be the difference between the squared strain rate and the squared vorticity. It therefore has a different sign in vorticity-dominated and strain-dominated regions of the flow and can be used to discriminate between elliptic points, which are found in strongly rotating regions, and hyperbolic points, which are found in straining regions. This procedure, however, was unable to handle high-shear regions correctly, since curvature is often high in these areas even without the presence of a hyperbolic or elliptic point. To demonstrate this effect, we show in Fig. 4 the results of the two algorithms applied to the Kolmogorov flow at low  $Re$ . Recall that the basic pattern of the Kolmogorov flow is a periodic sequence of parallel shear bands; above a critical  $Re$ , the flow passes through an instability and the pattern changes to a hexagonal vortex lattice. In Fig. 4,  $Re$  is just above its critical value, and so the flow still contains significant amounts of shear. To illustrate the flow, Fig. 4(a) shows the shear rate across the full field. In Fig. 4(b), we show the results of applying our previous algorithm, where we choose the mean curvature as our threshold. Along the lines of high shear, many spurious hyperbolic and elliptic points are found. In contrast, in Fig. 4(c) we show the results of the new method presented above.

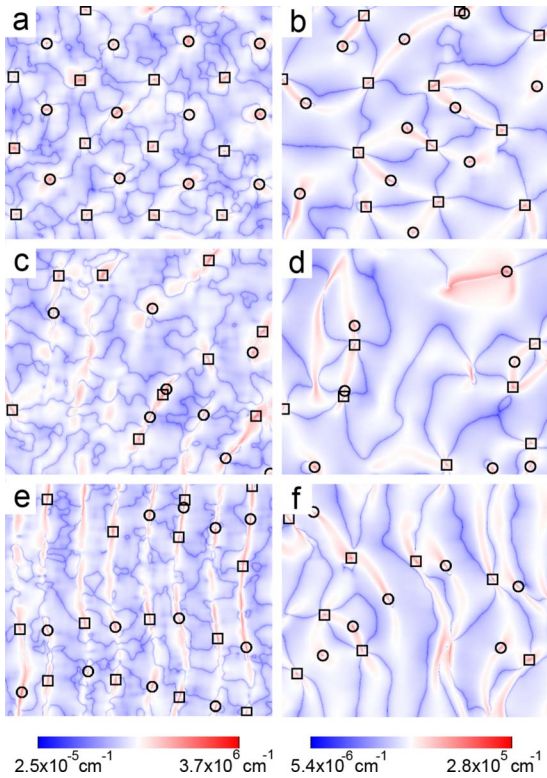


FIG. 5. (Color online) Curvature fields for each of the three flows, for the same data as in Fig. 3. The shading shows the logarithm of the curvature. Low-curvature regions tend to form linelike structures, while high curvatures appear as isolated points. The circles show the located elliptic points, while the squares mark hyperbolic points. Both are located at maxima of the curvature.

Many curvature maxima that were spuriously identified as hyperbolic and elliptic points in Fig. 4(b) now do not pass our topological test and are rejected. While we cannot be certain that all of the spurious points have been eliminated, the topological charge is clearly a better discriminator than the Okubo–Weiss parameter.

To further demonstrate the results of our improved algorithm, we show in Fig. 5 the curvature fields, with the hyperbolic and elliptic points identified, that correspond to the velocity fields shown in Fig. 3. In all cases, the large values of the curvature field are tightly localized spatially: the curvature maxima are very sharp. It is also intriguing to note that the very small curvatures, corresponding to regions where fluid elements move in nearly straight lines, form distinct lines. The density of these lines appears to decrease as  $Re$  increases. Their significance, however, is unclear.

### III. RESULTS

#### A. Curvature probability density functions

The statistics of curvature have previously been studied in three-dimensional turbulent flow,<sup>18,22</sup> and it was shown that the PDF of the curvature is extremely wide, spanning nearly ten orders of magnitude. In each of these studies, the PDF of curvature was found to exhibit power-law tails, with the low-curvature side scaling linearly in  $\kappa$ , while the high-curvature side scales as  $\kappa^{-5/2}$ . Xu *et al.* explained this behav-

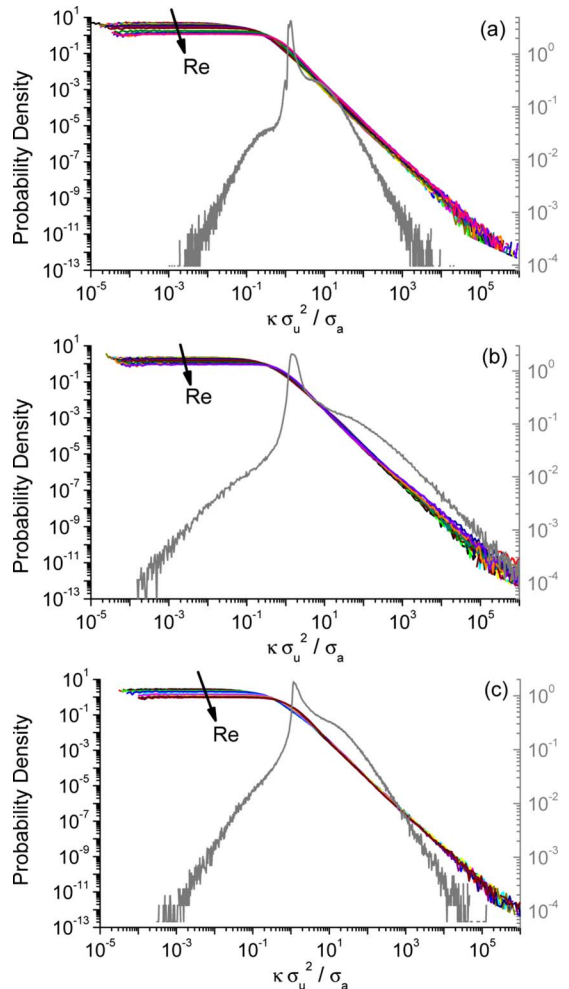


FIG. 6. (Color online) Curvature probability distributions (black lines) for each of the three flows; (a) square magnet lattice ( $28 \leq Re \leq 182$ ), (b) random magnet array ( $21 \leq Re \leq 168$ ), and (c) Kolmogorov flow ( $30 \leq Re \leq 201$ ). For each flow and for each Reynolds number, the PDF has a constant low-curvature tail and a high-curvature tail that scales as  $\kappa^{-2}$ . Data for different Reynolds numbers have been scaled by the appropriate combination of the velocity and acceleration variances, leading to a collapse of the data except at very small curvatures. The gray curves (right axes) show the curvature distribution measured only at the located hyperbolic and elliptic points, but combining data for all Reynolds numbers.

ior by constructing a simple model, where the Lagrangian velocity and acceleration were assumed to be Gaussian random variables.<sup>22</sup> In two dimensions, the power laws change; the model predicts a constant,  $\kappa^0$  low-curvature tail, and a  $\kappa^{-2}$  high-curvature tail.

Our measurements of the curvature PDFs are shown in Fig. 6 for each of the three flows investigated. In each case, we scale the curvature by  $\sigma_u^2/\sigma_a$ , where  $\sigma_u$  is the standard deviation of the velocity and  $\sigma_a$  is the standard deviation of the acceleration. For each flow, the data do not collapse perfectly with this rescaling; instead, there is a weak trend with Reynolds number. Surprisingly, we find the same  $\kappa^0$  and  $\kappa^{-2}$  power-law tails predicted by the two-dimensional version of the model of Xu *et al.*, even though the velocity and acceleration in our flows are certainly not random variables, particularly at low  $Re$ . Since the same PDF shape is found both

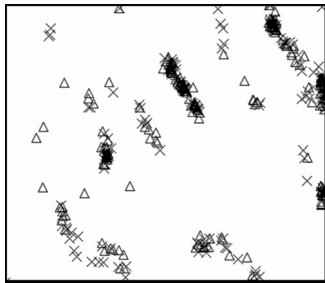


FIG. 7. Spatial dependence of the locations of creation (triangles) and annihilation (crosses) events for the random magnet array, for  $Re < 60$ . The creation and annihilation events are highly clustered and lie preferentially where the forcing in the time-independent regime produces hyperbolic and elliptic points that are very close together. Many of the recorded events for this flow at these low Reynolds numbers are spurious.

in our low-Re, time-independent flows and in high-Re turbulence, we conclude that the curvature statistics alone are insensitive to the flow details.

In Fig. 6, we also show the PDFs of the curvature measured at our located hyperbolic and elliptic points, with data from all Reynolds numbers averaged together to improve our statistics. These conditional PDFs show that, while it is more likely to find hyperbolic and elliptic points with curvature values in the decreasing, large-curvature tail, these features need only be local maxima, so some may be found in the flat, low-curvature part of the PDF. A thresholding-based detection algorithm, like the one we used previously,<sup>10</sup> is therefore a poor choice for locating hyperbolic and elliptic points. The improved method used here is significantly more robust.

## B. Hyperbolic/elliptic pair interactions

As  $Re$  increases, the flow pattern changes and becomes time dependent; that is, the symmetries of the forcing are spontaneously broken and the flow becomes spatiotemporally chaotic. If  $Re$  becomes high enough, the flow exhibits turbulence. In either of these cases, the velocity field changes in time and the locations of the hyperbolic and elliptic points are not static; rather, they move with the flow pattern. As we showed previously,<sup>10</sup> at low  $Re$ , they remain pinned to their forced locations, although they may move about these preferred sites. At high  $Re$ , however, they break free from these locations and wander over the flow. As they move, they interact; in particular, hyperbolic and elliptic points may annihilate in pairs, which corresponds physically to the merging of two vortices. New hyperbolic-elliptic pairs may also be nucleated when a vortex splits. We found previously with a square magnet lattice that these processes occur only above a critical  $Re$ . We propose that the presence of dynamically changing topology can be used as a defining characteristic of STC.<sup>10</sup> Fluctuations that do not change the flow topology represent a qualitatively weaker form of chaos.

We now consider these pair interactions for three distinct flows, applying our new methods for locating the hyperbolic and elliptic points. Once their positions are found, we use the same tracking algorithm normally used to determine the tracer-particle tracks to construct the trajectories of the hyperbolic and elliptic points. These trajectories then allow us

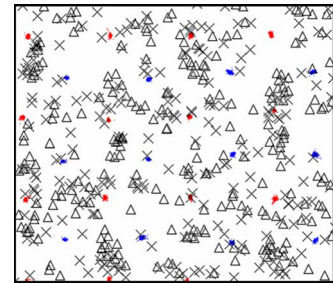


FIG. 8. (Color online) Spatial dependence of the locations of creation (triangles) and annihilation (crosses) events for the square magnet lattice, for all measured Reynolds numbers. The solid clusters show the trajectories of the hyperbolic and elliptic points at the lowest Reynolds number measured ( $Re = 28$ ), as a way to show the flow forcing. The creation and annihilation events appear to be uncorrelated with the flow forcing, and we believe that essentially all of them are real.

to find pair creation and annihilation events. Our criteria for identifying such events are simple. If the trajectories for a hyperbolic point and an elliptic point end at the same time step, and if at that time they were closer to each other than to any other points, we record an annihilation event. Similarly, if two trajectories start at the same time step and satisfy the nearness constraint, we record a creation.

The resolution with which we can locate the hyperbolic and elliptic points will, of course, affect our determination of creation and annihilation events. We estimate that we cannot distinguish hyperbolic and elliptic points separated by less than roughly 1 mm with our current spatial resolution; the annihilation of two points is therefore indistinguishable from their coming very close together. This resolution limit is an issue in our low-Re data from the random magnet array. Due to the particular magnet configuration, in the time-independent regime this flow contains hyperbolic and elliptic points that are very close together, near our resolution limit. As these nearby points begin to move, they come very close together, and we record a spurious annihilation event. When they then separate, we record a spurious creation event. That these events are not true creation and annihilation events is clearly shown in Fig. 7, where we plot the spatial distribution of creation and annihilation events for the random magnet array for  $Re < 60$ . The events are highly clustered and are well correlated with the locations of the nearby hyperbolic and elliptic points in the steady flow regime. As discussed above, as  $Re$  increases the hyperbolic and elliptic points are free to move. Since they are therefore no longer forced to be very close together, the number of spurious events is reduced. We note that spurious low-Re detection of creation and annihilation events is only a problem with our data from the random magnet array, where hyperbolic and elliptic points are forced to lie close together. For our other two forcing configurations, this problem is absent.

Indeed, for the square magnet lattice, pair creation and annihilation events are decorrelated from the flow forcing, as shown in Fig. 8 for all  $Re$  measured. These results suggest that the creation or annihilation of a hyperbolic/elliptic pair is not influenced by the base flow forcing, but instead is due

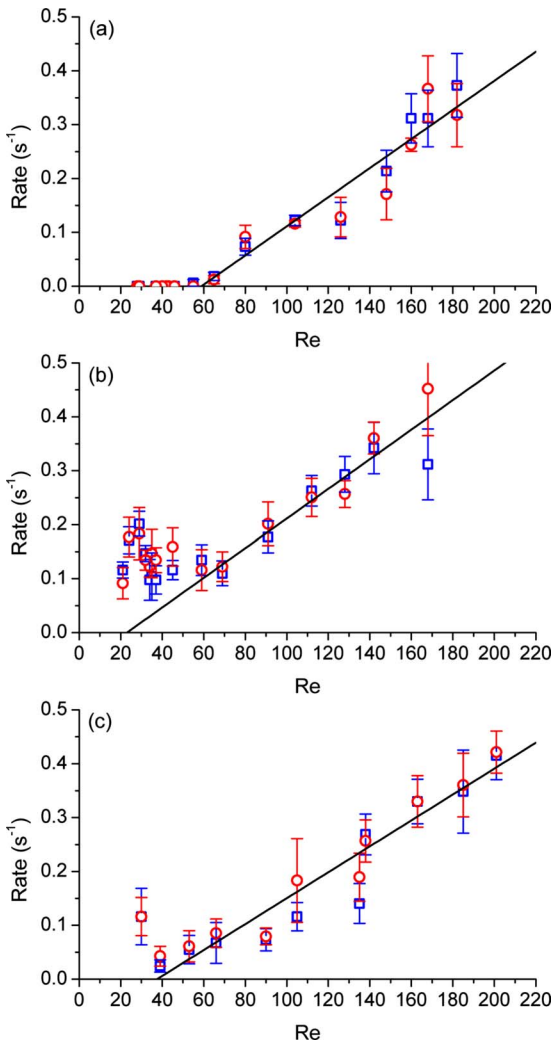


FIG. 9. (Color online) Rates of creation (squares) and annihilation (circles) of hyperbolic-elliptic point pairs for each of the three flows: (a) square magnet lattice, (b) random magnet array, and (c) Kolmogorov flow. The error bars are statistical and were determined by conducting several data runs and comparing the results. For each plot, the solid straight line is a linear fit to the data. In (b), the low Re ( $Re < 60$ ) data are ignored in the fit to avoid including spurious events.

to the dynamics of the flow, supporting our proposal that the changing topology can be regarded as the defining characteristic of STC.

We also find that the frequency of pairwise interactions rises as  $Re$  increases and the flow fluctuations become more important. In Fig. 9, we show the rates of pair creation and annihilation for each of the three flows. For the square magnet lattice [Fig. 9(a)], our results are similar to our previous finding: below a critical Reynolds number  $Re_c$ , there are no creation or annihilation events, and above  $Re_c$  the interaction rates increase rapidly. The shape of the curve is different here: whereas our previous results suggested a square-root-like rise of the interaction rates,<sup>10</sup> we here find a linear increase with  $Re$ . We attribute this difference to the improved detection methods presented in this paper. The hyperbolic and elliptic points become more difficult to locate and track as  $Re$  increases, and our earlier algorithms may not have resolved all the creation and annihilation events. Regardless

of the shape of the curve, however, the essential conclusion remains the same: below  $Re_c$ , the topology of the flow is fixed, while above  $Re_c$  it changes continually.

The flow forcing provided by the square magnet lattice has a considerable degree of symmetry, which is reflected in the flow pattern below  $Re_c$  [see, e.g., Fig. 3(a)]. Above  $Re_c$ , where the dynamics are spatiotemporally chaotic, the flow spontaneously breaks these symmetries. One might expect that when the flow forcing is less symmetric, less hydrodynamic kinetic energy would be required to break these symmetries and produce spatiotemporally chaotic flow, leading to a lower  $Re_c$ . To test this hypothesis, we measured the creation and annihilation rates in our other two flows, shown in Figs. 9(b) and 9(c). As with the square magnet lattice, the interaction rates rise linearly above some  $Re_c$ , as indicated by fits to the data. For the square magnet lattice, with periodic symmetry in two directions, we find that  $Re_c = 59 \pm 6$ . In contrast, the Kolmogorov flow has forcing symmetry in only one direction; its critical Reynolds number is lower, with  $Re_c = 37 \pm 6$ . Finally, the flow generated by the random magnet array, with no imposed spatial symmetry, has  $Re_c = 23 \pm 12$ . Note that for the random array, we include only creation and annihilation rates for  $Re < 60$ , where the methods are reliable, in determining  $Re_c$ .

#### IV. CONCLUSIONS

We have presented a method for locating the hyperbolic and elliptic points of a quasi-two-dimensional laboratory flow by using the curvature of tracer-particle trajectories. We have extended our prior work by studying three different forcing patterns with varying degrees of spatial symmetry. For each flow, hyperbolic and elliptic point pairs are nucleated or annihilated only above a critical Reynolds number. This critical Reynolds number is smaller for flows that are less symmetric. Apparently, less energy is required for the hyperbolic and elliptic points to break free from their forced locations when the flow symmetry is reduced. In contrast, the statistics (e.g., the PDF) of the curvature are almost identical for the three flows.

We propose that continually changing topology, represented by the creation and annihilation of hyperbolic/elliptic pairs, is an essential ingredient of STC; that is, systems with static topology are not spatiotemporally chaotic. We suggest that it might be fruitful to formulate models of STC based on topological dynamics of the kind discussed here.

#### ACKNOWLEDGMENTS

This work was supported by the U.S. National Science Foundation under Grant No. DMR-0405187.

<sup>1</sup>M. C. Cross and P. C. Hohenberg, "Pattern formation outside of equilibrium," *Rev. Mod. Phys.* **65**, 851 (1993).

<sup>2</sup>M. C. Cross and P. C. Hohenberg, "Spatiotemporal chaos," *Science* **263**, 1569 (1994).

<sup>3</sup>D. A. Egolf and H. S. Greenside, "Relation between fractal dimension and spatial correlation length for extensive chaos," *Nature (London)* **369**, 129 (1994).

<sup>4</sup>T. Bohr, E. Bosch, and W. van de Water, "Spatiotemporal chaos," *Nature (London)* **372**, 48 (1994).

<sup>5</sup>D. A. Egolf, I. V. Melnikov, W. Pesch, and R. E. Ecke, "Mechanisms of

- extensive spatiotemporal chaos in Rayleigh–Bénard convection,” *Nature (London)* **404**, 733 (2000).
- <sup>6</sup>S. W. Morris, E. Bodenschatz, D. S. Cannell, and G. Ahlers, “Spiral defect chaos in large aspect ratio Rayleigh–Bénard convection,” *Phys. Rev. Lett.* **71**, 2026 (1993).
- <sup>7</sup>E. Bodenschatz, W. Pesch, and G. Ahlers, “Recent developments in Rayleigh–Bénard convection,” *Annu. Rev. Fluid Mech.* **32**, 709 (2000).
- <sup>8</sup>M. Dennin, G. Ahlers, and D. S. Cannell, “Spatiotemporal chaos in electroconvection,” *Science* **272**, 388 (1996).
- <sup>9</sup>A. E. Perry and M. S. Chong, “A description of eddying motions and flow patterns using critical-point concepts,” *Annu. Rev. Fluid Mech.* **19**, 125 (1987).
- <sup>10</sup>N. T. Ouellette and J. P. Gollub, “Curvature fields, topology, and the dynamics of spatiotemporal chaos,” *Phys. Rev. Lett.* **99**, 194502 (2007).
- <sup>11</sup>G. A. Voth, G. Haller, and J. P. Gollub, “Experimental measurements of stretching fields in fluid mixing,” *Phys. Rev. Lett.* **88**, 254501 (2002).
- <sup>12</sup>G. A. Voth, T. C. Saint, G. Dobler, and J. P. Gollub, “Mixing rates and symmetry breaking in two-dimensional chaotic flow,” *Phys. Fluids* **15**, 2560 (2003).
- <sup>13</sup>J. M. Burgess, C. Bizon, W. D. McCormick, J. B. Swift, and H. L. Swinney, “Instability of the Kolmogorov flow in a soap film,” *Phys. Rev. E* **60**, 715 (1999).
- <sup>14</sup>J. Paret, D. Marteau, O. Paireau, and P. Tabeling, “Are flows electromagnetically forced in thin stratified layers two dimensional?” *Phys. Fluids* **9**, 3102 (1997).
- <sup>15</sup>D. Rothstein, E. Henry, and J. P. Gollub, “Persistent patterns in transient chaotic fluid mixing,” *Nature (London)* **401**, 770 (1999).
- <sup>16</sup>N. T. Ouellette, H. Xu, and E. Bodenschatz, “A quantitative study of three-dimensional Lagrangian particle tracking algorithms,” *Exp. Fluids* **40**, 301 (2006).
- <sup>17</sup>D. Vella and L. Mahadevan, “The Cheerios effect,” *Am. J. Phys.* **73**, 817 (2005).
- <sup>18</sup>W. Braun, F. De Lillo, and B. Eckhardt, “Geometry of particle paths in turbulent flows,” *J. Turbul.* **7**, 1 (2006).
- <sup>19</sup>J. F. Foss, “Surface selections and topological constraint evaluations for flow field analyses,” *Exp. Fluids* **37**, 883 (2004).
- <sup>20</sup>A. Okubo, “Horizontal dispersion of floatable particles in the vicinity of velocity singularities such as convergences,” *Deep-Sea Res.* **17**, 445 (1970).
- <sup>21</sup>J. B. Weiss, “The dynamics of the enstrophy transfer in two-dimensional turbulence,” *Physica D* **128**, 169 (1991).
- <sup>22</sup>H. Xu, N. T. Ouellette, and E. Bodenschatz, “Curvature of Lagrangian trajectories in turbulence,” *Phys. Rev. Lett.* **98**, 050201 (2007).